The Journal of
Chemical Physics

RESEARCH ARTICLE | FEBRUARY 18 2026

Analytical nuclear second derivatives for frozen-density embedding employing self-consistent field methods

Maximilian L. Kronenberger ; Sebastian Höfener

J. Chem. Phys. 164, 074105 (2026)
https://doi.org/10.1063/5.0308919

AIP Publishing

The Journal of Chemical Physics | ARTICLE | pubs.aip.org/aip/jcp

Analytical nuclear second derivatives for frozen-density embedding employing self-consistent field methods

Cite as: J. Chem. Phys. 164, 074105 (2026); doi: 10.1063/5.0308919
Submitted: 24 October 2025 • Accepted: 30 January 2026 •
Published Online: 18 February 2026

Maximilian L. Kronenberger and **Sebastian Höfener**[a)]

AFFILIATIONS

Institute of Physical Chemistry, Karlsruhe Institute of Technology (KIT), P.O. Box 6980, 76049 Karlsruhe, Germany

[a)] **Author to whom correspondence should be addressed:** hoefener@kit.edu

ABSTRACT

We report the derivation and implementation of analytical nuclear ground-state second derivatives for uncoupled frozen-density embedding (FDEu) within Hartree–Fock and Kohn–Sham density functional theory. Exchange integrals are evaluated using the chain-of-spheres exchange approach, for which exact nuclear second derivatives are derived and implemented, including all grid derivative contributions, to assess the accuracy of new approximate derivatives. The accuracy of the FDEu Hessian is assessed for selected sample systems by comparison with corresponding supermolecule calculations, encompassing both weakly and strongly coupled subsystems to investigate strengths and limitations of the approach. Finally, the vibrational frequencies of a naphthalene dimer embedded in a crystalline naphthalene environment—comprising up to 44 molecules and a total of 792 atoms—are presented, demonstrating the method's applicability to extended molecular systems and its potential for the conceptual analysis of intermolecular dimer vibrations relevant to charge transport.

I. INTRODUCTION

Organic semiconductors have attracted great interest due to their potential in flexible and lightweight electronic devices, such as organic field-effect transistors, light-emitting diodes, and photovoltaic cells.[1–5] Charge transport in organic semiconductors is strongly influenced by weak intermolecular interactions and low-frequency lattice vibrations, which can lead to energetic disorder and reduced carrier mobility. Such vibrations, sometimes referred to as "killer phonon modes," modulate the electronic coupling between neighboring molecules and thus play a decisive role in determining charge-transport properties.[6,7] To accurately describe these effects from first principles, access to molecular vibrational properties and their influence upon electronic properties in large, weakly bound molecular assemblies is essential.

Molecular vibrational properties are accessible via nuclear second derivatives of the electronic energy. Analytical implementations are of central importance as they provide results at a fraction of the computational cost and with higher accuracy compared to (semi-)numerical differentiation techniques. Ground-state self-consistent field (SCF) analytical nuclear second derivatives have been reported in the literature for Hartree–Fock (HF) and Kohn–Sham density functional theory (DFT)[8–10] as well as for correlation methods, such as Møller–Plesset perturbation theory and coupled cluster theory.[11–14] However, the computational cost of Hessian calculations increases steeply with system size, limiting their routine application to small- and medium-sized systems. To extend the applicability of computational methods with significant scaling to larger systems, subsystem approaches provide an alternative. For example, second analytical derivatives for QM/MM approaches have been developed in the literature.[15–17] The vibrational treatment becomes even more increasingly challenging for the treatment of complex systems beyond the harmonic approximation. Several partition schemes to address these challenges have been reported, ranging from fixed subspace transformations via flexible adaptions of subspaces to embedding approaches; see, for example, Refs. 18–20 and references therein.

Embedding techniques allow the evaluation of molecular properties for the active subsystem while retaining the essential influence of the environment at reduced cost compared to a supermolecular calculation. In the uncoupled frozen-density embedding (FDEu) QM/QM scheme, the total system is partitioned into an active subsystem and a frozen environment that interacts via an embedding potential, including electrostatic, exchange–correlation, nonadditive exchange correlation, and kinetic energy contributions.[21–25] FDEu Hessians are, therefore, particularly appealing for large assemblies where only local properties are of interest, such as vibrational effects on electronic properties in organic semiconductors. Ground-state analytical gradients have been reported previously for HF and DFT in the FDEu scheme.[26] Analytical gradients for related embedded wave function and DFT methods were claimed to be reported but without providing any equations.[27] Embedded gradients have furthermore been applied in *ab initio* molecular dynamics simulations[28] and in geometry optimizations.[29] However, to the best of our knowledge, analytical second derivatives for frozen-density embedding have not yet been presented with equations.

While the FDEu approach addresses the scaling of frequency calculations with system size in principle, an efficient implementation of the Hessian remains essential for treating larger subsystems. A well-established way to reduce computational cost of two-electron exchange integrals over Gaussian basis functions is chain-of-spheres exchange (COSX),[30–34] which is also referred to as seminumerical exchange. In this framework, two-electron exchange integrals are evaluated semi-numerically, i.e., the integration over one electron coordinate is performed numerically. This approach retains near-exact accuracy if appropriate integration grids are used.[35] The COSX method has been successfully applied to a variety of electronic structure methods and properties, including, e.g., SCF energy gradients,[30,31,36] time-dependent DFT calculations,[33,37] and molecular Hessians.[32] Exact analytical gradients of the COSX energy expression have been reported in the literature, along with efficient approximations that further reduce the computational scaling.[30,38] Nuclear second derivatives of the COSX energy have also been reported, albeit employing such approximations only.[32] To the best of our knowledge, exact analytical second derivatives of the COSX energy, including grid weight derivatives and grid Pulay contributions, have not yet been reported in the literature.

In the present work, we report the derivation and implementation of analytical nuclear second derivatives for the FDEu approach within both the HF and Kohn–Sham DFT frameworks. Exact analytical second derivatives of the COSX energy expression, including grid derivative contributions, are derived and implemented. The performance of the approximation to the nuclear second derivative of the COSX energy is then evaluated by direct comparison with the exact expressions.[32] Furthermore, the accuracy of the resulting FDEu Hessian is assessed for representative systems, including a naphthalene dimer inside a naphthalene cluster as an example to study the effect of local vibrations upon local frontier orbitals.

This article is organized as follows: First, we introduce the relevant theory in Sec. II, giving detailed expressions for the FDEu gradient and Hessian. First and second derivatives of the COSX energy are derived, including grid weight derivatives and grid Pulay terms, and approximations for the COSX contributions to the Hessian are reported. After reviewing the computational methods in Sec. III, results are provided in Sec. IV. The article closes with a summary and an outlook in Sec. V.

II. THEORY

In Sec. II A, analytical nuclear second derivatives are derived within the uncoupled frozen-density embedding framework. In Sec. II B, the COSX approximation for the intra-subsystem exact exchange is summarized, and its analytical first and second derivatives are reported including all relevant contributions. In the FDEu approach, no inter-subsystem exact exchange occurs, and the COSX method is, therefore, only employed as an efficient approximation in our implementation but without a direct relation to FDEu.

A. Frozen-density embedding

In the frozen-density embedding (FDE) approach, the total energy of the supersystem is expressed as the sum of the subsystem energies and an interaction energy,[21–25]

$$E_{\mathrm{tot}}[\rho(\mathbf{r})] = E_{\mathrm{I}}[\rho_{\mathrm{I}}(\mathbf{r})] + E_{\mathrm{int}}[\rho_{\mathrm{I}}(\mathbf{r}),\rho_{\mathrm{II}}(\mathbf{r})] + E_{\mathrm{II}}[\rho_{\mathrm{II}}(\mathbf{r})]. \tag{1}$$

Note that we limit the discussion to two substems for brevity, while FDE and its implementation are not limited to two subsystems. The interaction energy between subsystems is given as[39]

$$\begin{aligned} E_{\mathrm{int}}[\rho_{\mathrm{I}}(\mathbf{r}),\rho_{\mathrm{II}}(\mathbf{r})] = {} & \int \rho_{\mathrm{I}}(\mathbf{r})\, V_{\mathrm{nuc,II}}\,\mathrm{d}\mathbf{r} + \int \rho_{\mathrm{II}}(\mathbf{r})\, V_{\mathrm{nuc,I}}\,\mathrm{d}\mathbf{r} \\ & + E_{\mathrm{nuc,I/II}} + \iint \frac{\rho_{\mathrm{I}}(\mathbf{r})\rho_{\mathrm{II}}(\mathbf{r}')}{|\mathbf{r}-\mathbf{r}'|}\,\mathrm{d}\mathbf{r}\,\mathrm{d}\mathbf{r}' \\ & + E_{\mathrm{xck:nadd}}[\rho_{\mathrm{I}},\rho_{\mathrm{II}}], \end{aligned} \tag{2}$$

with the nuclear Coulomb potential of the respective subsystem X,

$$V_{\mathrm{nuc,X}} = -\sum_{A\in \mathrm{X}} \frac{Z_A}{|\mathbf{r}-\mathbf{R}_A|}. \tag{3}$$

The final term in Eq. (2) accounts for the non-additive contributions of exchange–correlation and kinetic energies, which arise due to the non-linear dependence of these terms on the electron density ρ. This term is formulated using DFT, independent of the specific methods used for the individual subsystems,

$$\begin{aligned} E_{\mathrm{xck:nadd}}[\rho_{\mathrm{I}},\rho_{\mathrm{II}}] = {} & E_{\mathrm{xc}}[\rho_{\mathrm{I}}+\rho_{\mathrm{II}}] - \sum_{z=\mathrm{I,II}} E_{\mathrm{xc}}[\rho_z] + T_s[\rho_{\mathrm{I}}+\rho_{\mathrm{II}}] \\ & - \sum_{z=\mathrm{I,II}} T_s[\rho_z]. \end{aligned} \tag{4}$$

For the remainder of this work, subsystem I will be active and subsystem II will be treated as a frozen environment. The closed-shell active density is computed from Gaussian-type basis functions ϕ contracted with the SCF density matrix $\mathbf{D}^{\mathrm{I}}$,

$$\rho_{\mathrm{I}}(\mathbf{r}) = \sum_{\mu\nu} D^{\mathrm{I}}_{\mu\nu}\phi_\mu(\mathbf{r})\phi_\nu(\mathbf{r}), \tag{5}$$

$$D^{\mathrm{I}}_{\mu\nu} = \sum_i 2\, C_{\mu i} C_{\nu i}, \tag{6}$$

where $C_{\mu i}$ are molecular orbital (MO) coefficients. The active subsystem experiences an embedding potential through the interaction with the environment, which is obtained as the derivative of the interaction energy with respect to the density matrix,

$$V^{\mathrm{emb,I}}_{\mu\nu} = \frac{\partial E_{\mathrm{int}}}{\partial D^{\mathrm{I}}_{\mu\nu}} = (\mu|V_{\mathrm{nuc,II}}|\nu) + J_{\mu\nu}[\rho_{\mathrm{II}}] + V^{\mathrm{xck:nadd}}_{\mu\nu}[\rho_{\mathrm{I}},\rho_{\mathrm{II}}]. \tag{7}$$

The Fock matrix of the active system contains both the embedding terms and the intrinsic contributions of the active subsystem,[40,41]

$$F_{\mu\nu} = F^{\mathrm{I}}_{\mu\nu} + V^{\mathrm{emb,I}}_{\mu\nu}, \tag{8}$$

$$F^{\mathrm{I}}_{\mu\nu} = h_{\mu\nu} + J_{\mu\nu}[\rho_{\mathrm{I}}] - c_{\mathrm{x}} K_{\mu\nu} + (1 - c_{\mathrm{x}}) V^{\mathrm{xc}}_{\mu\nu}. \tag{9}$$

Equation (9) comprises the usual one-electron matrix elements $h_{\mu\nu}$, Coulomb matrix elements $J_{\mu\nu}$, scaled Hartree–Fock (HF) exchange matrix elements $K_{\mu\nu}$, and exchange–correlation (xc) matrix elements $V^{\mathrm{xc}}_{\mu\nu}$. Here, c_{x} denotes the scaling factor determining the fraction of exact exchange included in the xc functional. Note that index I is dropped for some terms for better readability. Throughout this work, Greek indices $\mu, \nu, \kappa, \lambda$ indicate atomic Gaussian-type basis functions. General molecular orbital indices are denoted by p, q, r, s, while i, j, k, l refer to occupied MOs and a, b refer to virtual MOs.

1. Analytic nuclear gradient

To evaluate derivatives of the total FDE energy with respect to nuclear perturbations, the first step is the formulation of working equations for the FDE restricted Kohn–Sham (RKS) energy gradient. Although the analytical expression for the FDE energy gradient has been reported previously,[26] its derivation is summarized to introduce the notation and intermediate quantities required for the subsequent formulation of the second derivatives. In order to ensure computational efficiency, the response of the environment to the geometry perturbation ξ is neglected throughout this work, commonly referred to as uncoupled FDE (FDEu). As a consequence, only the density response of the active subsystem is considered. Differentiating Eq. (1) with respect to ξ yields in this approximation,

$$\frac{\mathrm{d}E_{\mathrm{tot}}}{\mathrm{d}\xi} = E^{(\xi)}_{\mathrm{I}} + E^{(\xi)}_{\mathrm{int}} + E_{\mathrm{I}}\left[D^{\xi}\right] + E_{\mathrm{int}}\left[D^{\xi}\right]. \tag{10}$$

Terms involving upper parentheses indicate that derivatives of MO coefficients are skipped in this particular term. Thus, the first two terms do not depend explicitly on the perturbed orbitals, while the latter two describe the response of the orbitals of subsystem I.

The first term in Eq. (10) corresponds to the conventional contributions in vacuum and, employing density fitting (DF) for the Coulomb energy, is given as

$$E^{(\xi)}_{\mathrm{I}} = \sum_{\mu\nu} D_{\mu\nu} h^{\xi}_{\mu\nu} + E^{(\xi)}_{\mathrm{DF}-J} + E^{(\xi)}_{K} + E^{\xi}_{\mathrm{nuc,I}} + E^{(\xi)}_{\mathrm{xc}}. \tag{11}$$

To give an example, the gradient contributions of the Coulomb energy and exchange energy, respectively, with the response of the orbitals not being included, are given as follows:

$$E^{(\xi)}_{\mathrm{DF}-J} = \frac{1}{2} \sum_{\mu\nu\kappa\lambda} D_{\mu\nu} D_{\kappa\lambda} (\mu\nu|\kappa\lambda)^{\xi}_{\mathrm{DF}}, \tag{12}$$

$$E^{(\xi)}_{K} = -\frac{1}{4} c_{\mathrm{x}} \sum_{\mu\nu\kappa\lambda} D_{\mu\nu} D_{\kappa\lambda} (\mu\kappa|\nu\lambda)^{\xi}. \tag{13}$$

The second term in Eq. (10) is given by

$$\begin{aligned} E^{(\xi)}_{\mathrm{int}} = E^{\xi}_{\mathrm{nuc,I/II}} + E^{(\xi)}_{\mathrm{xck:nadd}} + \sum_{\mu\nu} D_{\mu\nu} (\mu|V_{\mathrm{nuc,II}}|\nu)^{\xi} + \int \rho_{\mathrm{II}}\, V^{\xi}_{\mathrm{nuc,I}} \mathbf{dr} \\ + \sum_{g} w_g \sum_{\mu\nu} D_{\mu\nu} (\phi_{\mu g} \phi_{\nu g})^{\xi} J_g[\rho_{\mathrm{II}}], \end{aligned} \tag{14}$$

where the electron–electron and electron–nuclear interaction between the active subsystem and the environment are evaluated on a supermolecular grid. Here, w_g is the weight of grid point g, and $\mathbf{r}_g$ is its coordinate. The Coulomb potential generated by electrons of the environment can be expressed as

$$J_g[\rho_{\mathrm{II}}] = \sum_{\kappa\lambda} D^{\mathrm{II}}_{\kappa\lambda} (\kappa|\lambda)_g, \tag{15}$$

with the two-index Coulomb integral,

$$(\kappa|\lambda)_g = \int \mathbf{d}\mathbf{r} \frac{\phi_\kappa(\mathbf{r}) \phi_\lambda(\mathbf{r})}{|\mathbf{r} - \mathbf{r}_g|}. \tag{16}$$

The electron density and the Coulomb potential of the environment are evaluated as part of the freeze-and-thaw procedure and are stored for each grid point.[26] They are read from a file and are kept unchanged for the gradient calculation of the target subsystem.

Finally, terms containing the perturbed density matrix of the active subsystem in Eq. (10) can be collected as

$$E_{\mathrm{I}}\left[D^{\xi}\right] + E_{\mathrm{int}}\left[D^{\xi}\right] = -\sum_{\mu\nu} W_{\mu\nu} S^{\xi}_{\mu\nu}, \tag{17}$$

where $\mathbf{W}$ denotes the energy weighted density matrix,

$$W_{\mu\nu} = \sum_{i} 2\, \varepsilon_i C_{\mu i} C_{\nu i}, \tag{18}$$

ε_i denotes orbital energies, and $\mathbf{S}^{\xi}$ is the derivative overlap matrix. This expression exploits the orthonormality condition of the molecular orbitals, which leads to a cancellation of the orbital response terms so that orbital rotation matrices are avoided in the gradient evaluation.[8] Finally, the FDEu SCF energy gradient can be cast in the usual form[26]

$$\frac{\mathrm{d}E_{\mathrm{tot}}}{\mathrm{d}\xi} = E^{(\xi)}_{\mathrm{I}} + E^{(\xi)}_{\mathrm{int}} - \sum_{\mu\nu} W_{\mu\nu} S^{\xi}_{\mu\nu}. \tag{19}$$

2. Analytic nuclear second derivatives

Starting from the gradient in Eq. (19), further differentiation with respect to a second nuclear Cartesian component χ yields the target FDEu Hessian,

$$\begin{aligned} \frac{\mathrm{d}^2 E_{\mathrm{tot}}}{\mathrm{d}\chi \mathrm{d}\xi} = E^{(\chi)(\xi)}_{\mathrm{I}} - \sum_{\mu\nu} W_{\mu\nu} S^{\chi\xi}_{\mu\nu} - 2 \sum_{ij} F^{(\chi)}_{ij} S^{(\xi)}_{ij} \\ + 4 \sum_{pi} U^{\chi}_{pi} \mathrm{RHS}^{(\xi)}_{pi} + E^{(\chi)(\xi)}_{\mathrm{int}}. \end{aligned} \tag{20}$$

Note that terms with upper parentheses indicate derivatives taken at constant molecular orbital coefficients. For example, the first derivative of the overlap matrix in the MO basis reads

$$S^{(\xi)}_{pq} = \sum_{\mu\nu} C_{\mu p} S^{\xi}_{\mu\nu} C_{\nu q}. \tag{21}$$

The coupled-perturbed Kohn–Sham (CPKS) equation's right-hand side (RHS) is given as

$$\mathrm{RHS}_{pi}^{(\xi)} = F_{pi}^{(\xi)} - \varepsilon_i S_{pi}^{(\xi)} - \frac{1}{2}\sum_{kl} S_{kl}^{(\xi)} A_{pikl}. \tag{22}$$

The RKS FDEu coupling matrix **A** in its general form is[26]

$$\begin{aligned} A_{pqrs} = {} & 4(pq|rs)_{\mathrm{DF}} - c_{\mathrm{x}}(pr|qs) - c_{\mathrm{x}}(\mathrm{ps}|qr) + 2(1-c_{\mathrm{x}})K_{pqrs}^{\mathrm{xc}} \\ & + 2K_{pqrs}^{\mathrm{xck:nadd}}, \end{aligned} \tag{23}$$

where K^{xc} and $K^{\mathrm{xck:nadd}}$ denote the usual exchange–correlation and non-additive kinetic energy exchange–correlation kernels,[40] respectively. Orbital rotations within the occupied-virtual block are obtained as solution to the CPKS equations,[8,10,42,43]

$$-\mathrm{RHS}_{ai}^{(\chi)} = \sum_{bj}\left[(\varepsilon_a - \varepsilon_i)\delta_{ij}\delta_{ab} + A_{aibj}\right]U_{bj}^{\chi}, \tag{24}$$

which are routinely solved using Davidson's method in an iterative fashion.[44] The occupied–occupied orbital rotations U_{ji}^{χ} are defined in terms of the derivative overlap matrix as

$$U_{ji}^{\chi} = -\frac{1}{2}S_{ji}^{(\chi)}. \tag{25}$$

The structure of Eq. (20) looks very similar to the KS DFT Hessian,[10] with only the second derivative of the interaction energy explicitly arising as an additional term. The first term in Eq. (20) only contains conventional contributions,[10]

$$E_{\mathrm{I}}^{(\chi)(\xi)} = \sum_{\mu\nu} D_{\mu\nu}h_{\mu\nu}^{\chi\xi} + E_{\mathrm{DF}-J}^{(\chi)(\xi)} + E_{K}^{(\chi)(\xi)} + E_{\mathrm{nuc,I}}^{\chi\xi} + E_{\mathrm{xc}}^{(\chi)(\xi)}, \tag{26}$$

and for the sake of completeness, the second derivative of the electronic Coulomb term employing density fitting (DF), as implemented, is given in the Appendix. At first glance, the last term in Eq. (20) seems to include all contributions from the interaction energy,

$$\begin{aligned} E_{\mathrm{int}}^{(\chi)(\xi)} = {} & E_{\mathrm{nuc,I/II}}^{\chi\xi} + E_{\mathrm{xck:nadd}}^{(\chi)(\xi)} + \sum_{\mu\nu} D_{\mu\nu}(\mu|V_{\mathrm{nuc,II}}|\nu)^{\chi\xi} \\ & + \int \rho_{\mathrm{II}}\, V_{\mathrm{nuc,I}}^{\chi\xi}\mathrm{d}\mathbf{r} + \sum_{g} w_g \sum_{\mu\nu} D_{\mu\nu}(\phi_{\mu g}\phi_{\nu g})^{\chi\xi} J_g[\rho_{\mathrm{II}}]. \end{aligned} \tag{27}$$

Note, however, that the embedding potential and embedding kernel enter the expressions in many places since such contributions are, e.g., included in the Fock matrix, cf. Eq. (8), and the coupling matrix **A**, cf. Eq. (23).

B. Seminumerical exchange

Having discussed analytical nuclear second derivatives for FDEu, efficient schemes for intra-molecular contributions are desirable, which are independent of environment contributions. For example, the use of density fitting for intra-molecular Coulomb contributions is employed, cf. Appendix. For an efficient treatment of the intra-molecular exact exchange contributions, we have chosen to employ the COSX approximation in which the integration over one electron coordinate is replaced by a numerical integration on a grid. The exchange contributions to the closed-shell energy then become

$$E_{K,\,\mathrm{sem}} = -\frac{1}{4}c_{\mathrm{x}}\sum_{\mu\nu\kappa\lambda} D_{\mu\nu}D_{\kappa\lambda}(\mu\kappa|\nu\lambda)_{\mathrm{sem}}, \tag{28}$$

where the two-electron integral is approximated as follows:

$$(\mu\kappa|\nu\lambda)_{\mathrm{sem}} = \sum_{g} w_g\, \phi_{\mu g}\, \phi_{\kappa g}\, (\nu|\lambda)_g = \sum_{g} f_g(\mathbf{R}_I, \mathbf{R}_J, \ldots, \mathbf{r}_g), \tag{29}$$

with the grid weight being w_g, the Gaussian basis functions evaluated at the grid point coordinate being $\phi_{\mu g} \equiv \phi_\mu(\mathbf{r}_g)$, and the two-index integral being $(\nu|\lambda)_g$, cf. Eq. (16). Note that the quantity f_g depends on the atomic orbitals $\mu\,\nu, \kappa\,\lambda$ but we have decided to drop those in our shorthand notation for better readability.

1. Gradient

The evaluation of first- and second-order energy derivatives, as well as derivatives of the Fock matrix, requires derivatives of two-electron exchange integrals. For instance, the exchange contributions to the gradient in Eq. (13) are obtained using differentiated seminumerical exchange integrals,

$$E_{K,\,\mathrm{sem}}^{(\xi)} = -\frac{1}{4}c_{\mathrm{x}}\sum_{\mu\nu\kappa\lambda} D_{\mu\nu}D_{\kappa\lambda}(\mu\kappa|\nu\lambda)_{\mathrm{sem}}^{\xi}. \tag{30}$$

The seminumerical integration is carried out on an atom-centered grid, where grid points $\mathbf{r}_g$ directly depend on the position of the respective nucleus $\mathbf{R}_G$ they are centered on, via

$$\mathbf{r}_g = \mathbf{r}' + \mathbf{R}_G. \tag{31}$$

Differentiating a finite grid, as occurring in f_g in Eq. (29), with respect to a nuclear Cartesian coordinate $R_{I\alpha} \equiv \xi$, derivatives of $\mathbf{r}_g$ also have to be taken into account,[45]

$$(\mu\kappa|\nu\lambda)_{\mathrm{sem}}^{\xi} \equiv \frac{d(\mu\kappa|\nu\lambda)_{\mathrm{sem}}}{dR_{I\alpha}} = \sum_{g}\left(\frac{\partial f_g}{\partial R_{I\alpha}} + \frac{\partial f_g}{\partial\, r_{g\alpha}}\frac{\partial\, r_{g\alpha}}{\partial R_{I\alpha}}\right). \tag{32}$$

In the present work, the second term in parentheses will be referred to as grid Pulay correction. It describes the gradient contribution occurring due to the dependence of the grid point on the nuclear coordinate. This term only gives non-zero contributions for derivatives with respect to the nuclear coordinate $\mathbf{R}_G$ on which the grid point is centered,

$$\frac{\partial\, r_{g\alpha}}{\partial R_{I\alpha}} = \delta_{IG}, \tag{33}$$

leading to the expression for the grid Pulay term,

$$\frac{\partial f_g}{\partial\, r_{g\alpha}}\frac{\partial\, r_{g\alpha}}{\partial R_{I\alpha}} = \delta_{IG}\frac{\partial f_g}{\partial r_{g\alpha}}. \tag{34}$$

This derivative of f_g formally requires differentiation of the two-index Coulomb integrals in Eq. (16), involving computationally demanding integrals over the differentiated operator. However, such terms can be avoided entirely, realizing that f_g only depends on $\mathbf{r}_g$ through relative coordinates $|\mathbf{r}_g - \mathbf{R}_J|$. Consequently, the derivative of f_g with respect to a grid point can be replaced by a sum over all derivatives with respect to nuclear coordinates $\mathbf{R}_A$,

$$\frac{\partial f_g}{\partial r_{g\alpha}} = -\sum_A \frac{\partial f_g}{\partial R_{A\alpha}}. \tag{35}$$

Finally, the integral derivative is obtained as

$$\frac{d(\mu\kappa|\nu\lambda)_{\text{sem}}}{dR_{I\alpha}} = \sum_g \left(\frac{\partial f_g}{\partial R_{I\alpha}} - \delta_{IG} \sum_A \frac{\partial f_g}{\partial R_{A\alpha}} \right). \tag{36}$$

This reduces the computational effort to the evaluation of derivatives of f_g with respect to nuclear Cartesian coordinates $R_{J\alpha}$,

$$\begin{aligned} \frac{\partial f_g}{\partial R_{J\alpha}} &= \frac{\partial w_g}{\partial R_{J\alpha}} \phi_{\mu g} \phi_{\kappa g} (\nu|\lambda)_g + w_g \frac{\partial \phi_{\mu g}}{\partial R_{J\alpha}} \phi_{\kappa g} (\nu|\lambda)_g \\ &\quad + w_g \phi_{\mu g} \frac{\partial \phi_{\kappa g}}{\partial R_{J\alpha}} (\nu|\lambda)_g + w_g \phi_{\mu g} \phi_{\kappa g} \frac{\partial (\nu|\lambda)_g}{\partial R_{J\alpha}}, \end{aligned} \tag{37}$$

which accounts for grid weight derivatives, derivatives of the basis functions, and derivatives of the two-index Coulomb integrals.

2. Hessian

Exchange contributions to the Hessian also require second derivatives of two-electron exchange integrals,

$$E^{(\chi)(\xi)}_{K,\,\text{sem}} = -\frac{1}{4} c_{\text{x}} \sum_{\mu\nu\kappa\lambda} D_{\mu\nu} D_{\kappa\lambda} (\mu\kappa|\nu\lambda)^{\chi\xi}_{\text{sem}}. \tag{38}$$

Differentiation of the first derivative integrals in Eq. (36) with respect to a second nuclear Cartesian coordinate $R_{J\beta} \equiv \chi$ yields the required second derivative exchange integral,

$$\begin{aligned} \frac{d}{dR_{J\beta}} \frac{d(\mu\kappa|\nu\lambda)_{\text{sem}}}{dR_{I\alpha}} &= \sum_g \frac{\partial^2 f_g}{\partial R_{J\beta} \partial R_{I\alpha}} - \sum_g \delta_{IG} \sum_A \frac{\partial^2 f_g}{\partial R_{J\beta} \partial R_{A\alpha}} \\ &\quad - \sum_g \delta_{JG} \sum_B \frac{\partial^2 f_g}{\partial R_{B\beta} \partial R_{I\alpha}} \\ &\quad + \sum_g \delta_{JG} \delta_{IG} \sum_B \sum_A \frac{\partial^2 f_g}{\partial R_{B\beta} \partial R_{A\alpha}}. \end{aligned} \tag{39}$$

Here, the grid Pulay contributions are again expressed via partial derivatives with respect to nuclear displacements, cf. Eq. (35). Thus, computationally demanding two-index Coulomb integrals over the differentiated operator are avoided. However, this expression requires first and second grid weight derivatives as well as derivatives of the two-index integrals in Eq. (16) and the basis functions up to second order.

Note that the CPKS RHS in Eq. (22) requires first derivative exchange integrals, which are evaluated using the seminumerical scheme outlined in Eq. (36) throughout this work, including grid weight derivative and grid Pulay terms.

3. Approximate gradient and Hessian

Up to this point, the exact gradient and exact Hessian of the seminumerical exchange energy were addressed in Eqs. (30) and (38), respectively. However, differentiating the original exchange energy, cf. Eq. (13), can be cast as[30,38]

$$E^{(\xi)}_K = -c_{\text{x}} \sum_{\mu\nu\kappa\lambda} D_{\mu\nu} D_{\kappa\lambda} \left(\mu^\xi \kappa | \nu\lambda \right), \tag{40}$$

which can be approximated using seminumerical exchange,

$$E^{(\xi)}_K \approx -c_{\text{x}} \sum_g w_g \sum_{\mu\nu\kappa\lambda} D_{\mu\nu} D_{\kappa\lambda} \left(\frac{\partial \phi_{\mu g}}{\partial R_{I\alpha}} \right) \phi_{\kappa g} \, (\nu|\lambda)_g. \tag{41}$$

In such a scheme, the analytic gradient is formulated exactly and subsequently simplified by exploiting symmetry, followed by introducing the seminumerical exchange approximation in a second step. By doing so, integral derivatives, grid Pulay terms, and grid weight derivatives are completely avoided, requiring only basis function derivatives to evaluate the gradient. However, it should be stressed that the gradient obtained with Eq. (41) is not the exact derivative of the seminumerical exchange energy in Eq. (28). This approximation becomes equivalent to Eq. (30) only for a complete integration grid, but it was demonstrated that such an approximation yields accurate results while reducing computation times significantly.[38] A similar approximation can be applied to first derivative seminumerical exchange contributions to the Fock matrix derivatives required for constructing the CPKS RHS.[32] In the present work, however, the exact expression in Eq. (36), including grid weight derivatives and grid Pulay terms, is employed instead.

Analogous approximations can be considered for the second derivative of exchange integrals. The exchange type Hessian contributions can generally be cast as[32]

$$\begin{aligned} E^{(\chi)(\xi)}_K &= -\frac{1}{4} c_{\text{x}} \sum_{\mu\nu\kappa\lambda} D_{\mu\nu} D_{\kappa\lambda} (\mu\kappa|\nu\lambda)^{\chi\xi} = -c_{\text{x}} \sum_{\mu\nu\kappa\lambda} D_{\mu\nu} D_{\kappa\lambda} \\ &\quad \times \left\{ \left(\mu^{\chi\xi} \kappa | \nu\lambda \right) + \left(\mu^\chi \kappa^\xi | \nu\lambda \right) + \left(\mu^\chi \kappa | \nu^\xi \lambda \right) + \left(\mu^\chi \kappa | \nu\lambda^\xi \right) \right\}. \end{aligned} \tag{42}$$

In this case, inserting the seminumerical approach leads to

$$\begin{aligned} E^{(\chi)(\xi)}_K &\approx -c_{\text{x}} \sum_g w_g \sum_{\mu\nu} D_{\mu\nu} \Bigg\{ \phi^{\chi\xi}_{\mu g} \sum_{\kappa\lambda} D_{\kappa\lambda} \, \phi_{\kappa g} (\nu|\lambda) + \phi^\chi_{\mu g} \\ &\quad \times \sum_{\kappa\lambda} D_{\kappa\lambda} \, \phi^\xi_{\kappa g} (\nu|\lambda) + \phi^\chi_{\mu g} \sum_{\kappa\lambda} D_{\kappa\lambda} \, \phi_{\kappa g} \left(\nu^\xi | \lambda \right) \\ &\quad + \phi^\chi_{\mu g} \sum_{\kappa\lambda} D_{\kappa\lambda} \, \phi_{\kappa g} \left(\nu | \lambda^\xi \right) \Bigg\}, \end{aligned} \tag{43}$$

so that second derivatives of two-index integrals, grid weight derivatives, and grid Pulay corrections are completely avoided. The approximation in Eq. (43) will be investigated by comparison with the exact seminumerical Hessian contribution in Eq. (38) in Sec. IV A.

Bykov *et al.* have previously derived a similar expression, but they included second derivatives of the two-index integrals instead of second derivatives of basis functions. The authors argue that their approach leads to a more numerically stable procedure at the expense of a larger computational effort.[32]

III. COMPUTATIONAL DETAILS

The approaches for calculating exchange gradient contributions within the seminumerical exchange approach, given in Eqs. (30) and (41), were implemented into the program package KOALA. Furthermore, the seminumerical evaluation of first derivative exchange integrals, including grid weight derivatives and grid Pulay terms, was implemented for the construction of the CPKS RHS and will be used throughout this work for Hessian calculations. An overview of the integration grids in KOALA is given in the supplementary material. The numerical grids employed in this work were constructed following the scheme of Treutler and Ahlrichs,[46] combining Becke's partitioning[47] with a Chebyshev quadrature for the radial integration. For the angular part, Lebedev grids[48–50] were used even for finer grids, instead of the Lobatto grids originally proposed. To assess the accuracy of the different approaches for computing second derivatives of seminumerical exchange, calculations were performed for a test set of 41 organic molecules, constituting a subset of a 47-molecule benchmark set that has been employed in related studies.[31,32,51,52]

All embedding calculations have been carried out with the program package KOALA[53] using PBE[54] as the xc functional and PW91k[55] as the kinetic energy functional. The xc functional for the non-embedding type contributions may deviate and is stated for such cases. Coulomb integrals were evaluated employing the density fitting approximation (DF) in combination with Weigend's universal auxiliary basis sets throughout this work.[56,57] Supermolecule geometries were optimized with TURBOMOLE[58] at the respective level of theory. In all cases, these supermolecule geometries were used unchanged for the subsequent FDEu calculations.

Simulated vibrational spectra were generated using Lorentzian broadening with a full width at half maximum (FWHM) of 20 cm^{-1}, unless stated otherwise.

Displaced geometries were obtained by scaling the normal modes as follows: In our notation, $\mathbf{q}_m$ is the non-mass-weighted vector along the direction of normal mode m and μ_m is the corresponding reduced mass,

$$\mu_m = \frac{1}{|\mathbf{q}_m|^2}. \tag{44}$$

The dimensionless displacement vector is then given as

$$\mathbf{Q}_m = \mu_m^{1/2}\mathbf{q}_m. \tag{45}$$

For the quantum and thermic harmonic oscillator, the amplitude is expressed using the respective standard deviation,

$$\sigma_m^{\mathrm{quant}} = \sqrt{\langle x^2\rangle - \langle x\rangle^2} = \sqrt{\frac{\hbar}{2\mu_m\omega_m}}, \tag{46}$$

$$\sigma_m^{\mathrm{therm}} = \sqrt{\frac{k_B T}{\mu_m\omega_m^2}}, \tag{47}$$

where ω_m is the vibrational frequency of mode m. For the thermic approach, we have used 300 K in the current work. The displaced geometries were obtained for both cases as

$$x_m = \sigma_m\sqrt{2}\mathrm{erf}^{-1}(P), \tag{48}$$

$$\mathbf{R}_m = \mathbf{R}_0 \pm x_m\,\mathbf{Q}_m, \tag{49}$$

where $\mathbf{R}_0$ are the equilibrium coordinates. We have used $P = 95.45\%$, which corresponds to 2σ in the Gauß function in the ground state of the harmonic oscillator.

The directional derivative of an orbital energy,

$$\alpha_{z,m} = \frac{\mathrm{d}\varepsilon_z}{\mathrm{d}\mathbf{Q}_m}, \tag{50}$$

was obtained as the dot product of the gradient of ε_z,[59] with the dimensionless normalized displacement vector $\mathbf{Q}_m$,

$$\frac{\mathrm{d}\varepsilon_z}{\mathrm{d}\mathbf{Q}_m} = \sum_{\chi} g_{\chi,z}\,Q_{\chi,m}, \tag{51}$$

where $\boldsymbol{g}_z$ is the unnormalized gradient vector of the orbital energy of orbital z,

$$g_{\chi,z} = \frac{\mathrm{d}\varepsilon_z}{\mathrm{d}\chi}. \tag{52}$$

IV. RESULTS

This section presents an assessment of methods for nuclear second derivative seminumerical exchange contributions and a validation of the FDEu Hessian implementation. First, different approaches for computing second derivative seminumerical exchange contributions to the Hessian are analyzed, with particular attention paid to the validity of the approximation in Eq. (43). Second, the FDEu Hessian implementation is validated for a set of systems designed to probe both weak and strong geometric couplings between the active subsystem and its environment. Finally, the applicability of the method to molecules in complex environments containing a few hundred atoms is demonstrated.

A. Second derivative of seminumerical exchange integrals

In the present work, we refrain from further analysis of the seminumerical exchange gradient contributions since the validity of the approximation in Eq. (41) has been shown elsewhere.[32,38] We restrict our discussion to second derivatives of the seminumerical exchange energy and its respective approximation. The two approaches for calculating exchange contributions to the Hessian using seminumerical exchange, given in Eqs. (38) and (43), respectively, were implemented in KOALA and will be analyzed in the following.

We begin by calculating the vibrational frequencies of $\mathrm{CH_2Cl_2}$ at the HF/def2-SVP[60] level of theory using seminumerical exchange with a range of grid sizes. The molecular orbitals were obtained employing a fine grid 7 and kept fixed throughout all calculations in Table I. The root-mean-square deviations (RMSD) $|\Delta\tilde{\nu}|_{\mathrm{RMSD}}$ and mean-absolute deviations (MAD) $|\Delta\tilde{\nu}|_{\mathrm{MAD}}$ of the computed wavenumbers in cm^{-1} are summarized in Table I and are depicted in Fig. 1. Reference values were generated using the second derivative seminumerical exchange expression in Eq. (38), including grid weight derivatives and grid Pulay terms, in combination with a very fine reference grid RF. These values have served as reference for

TABLE I. Root mean square deviations (RMSD) and mean absolute deviations (MAD) in cm^{-1} of CH_2Cl_2 vibrations at the HF/def2-SVP level, obtained with four different schemes for evaluating second derivative seminumerical exchange contributions to the Hessian across various integration grids. Vibrational frequencies generated using method **A** with grid RF are used as references for the RMSD and MAD values.

	Method **A**		Method **A′**		Method **B**		Method **C**	
Grid	$\lvert\Delta\tilde{\nu}\rvert_{\text{RMSD}}$	$\lvert\Delta\tilde{\nu}\rvert_{\text{MAD}}$	$\lvert\Delta\tilde{\nu}\rvert_{\text{RMDS}}$	$\lvert\Delta\tilde{\nu}\rvert_{\text{MAD}}$	$\lvert\Delta\tilde{\nu}\rvert_{\text{RMSD}}$	$\lvert\Delta\tilde{\nu}\rvert_{\text{MAD}}$	$\lvert\Delta\tilde{\nu}\rvert_{\text{RMSD}}$	$\lvert\Delta\tilde{\nu}\rvert_{\text{MAD}}$
7	$3.20 \cdot 10^{-2}$	$2.22 \cdot 10^{-2}$	$8.81 \cdot 10^{-1}$	$7.62 \cdot 10^{-1}$	$1.74 \cdot 10^{0}$	$1.51 \cdot 10^{0}$	$2.19 \cdot 10^{-2}$	$1.89 \cdot 10^{-2}$
6	$7.54 \cdot 10^{-2}$	$4.89 \cdot 10^{-2}$	$6.16 \cdot 10^{0}$	$5.32 \cdot 10^{0}$	$1.23 \cdot 10^{1}$	$1.06 \cdot 10^{1}$	$2.19 \cdot 10^{-2}$	$1.89 \cdot 10^{-2}$
5	$1.31 \cdot 10^{-1}$	$9.89 \cdot 10^{-2}$	$2.28 \cdot 10^{1}$	$1.97 \cdot 10^{1}$	$4.64 \cdot 10^{1}$	$3.99 \cdot 10^{1}$	$2.19 \cdot 10^{-2}$	$1.89 \cdot 10^{-2}$
4	$2.23 \cdot 10^{-1}$	$1.87 \cdot 10^{-1}$	$1.88 \cdot 10^{2}$	$1.62 \cdot 10^{2}$	$3.35 \cdot 10^{2}$	$2.91 \cdot 10^{2}$	$2.19 \cdot 10^{-2}$	$1.89 \cdot 10^{-2}$
3	$5.54 \cdot 10^{-1}$	$4.49 \cdot 10^{-1}$	$8.47 \cdot 10^{2}$	$7.41 \cdot 10^{2}$	$1.35 \cdot 10^{3}$	$1.19 \cdot 10^{3}$	$2.11 \cdot 10^{-2}$	$1.78 \cdot 10^{-2}$
2	$3.18 \cdot 10^{0}$	$2.27 \cdot 10^{0}$	$1.73 \cdot 10^{3}$	$1.52 \cdot 10^{3}$	$2.68 \cdot 10^{3}$	$2.32 \cdot 10^{3}$	$2.58 \cdot 10^{-2}$	$2.00 \cdot 10^{-2}$
1	$4.64 \cdot 10^{0}$	$4.10 \cdot 10^{0}$	$1.92 \cdot 10^{3}$	$1.48 \cdot 10^{3}$	$2.71 \cdot 10^{3}$	$2.02 \cdot 10^{3}$	$1.62 \cdot 10^{-1}$	$1.40 \cdot 10^{-1}$
0	$3.81 \cdot 10^{1}$	$2.11 \cdot 10^{1}$	$9.91 \cdot 10^{3}$	$7.50 \cdot 10^{3}$	$1.37 \cdot 10^{4}$	$1.03 \cdot 10^{4}$	$2.30 \cdot 10^{-1}$	$1.66 \cdot 10^{-1}$

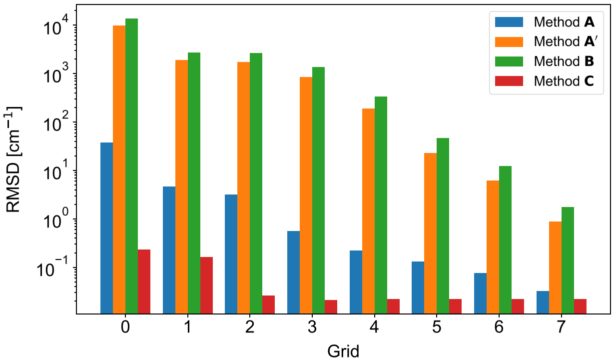

FIG. 1. Root mean square deviations (RMSD) in cm^{-1} of CH_2Cl_2 vibrations at the HF/def2-SVP level, obtained with four different schemes for evaluating second derivative seminumerical exchange contributions to the Hessian across various integration grids.

the calculation of RMSD and MAD values in Table I. All calculated vibrational frequencies are given in the supplementary material.

Four different schemes were employed for the evaluation of the second derivative seminumerical exchange contributions to the Hessian. The first approach is denoted method **A** in the present work. In this approach, the exact seminumerical exchange contributions given in Eq. (38) were used, including both grid Pulay terms and grid weight derivatives. The corresponding results are reported in the first two columns of Table I. For comparison, a simplified variant, denoted method **A′**, was considered, where grid Pulay and grid weight derivative contributions were omitted. The results of this poor-man's approach are reported in columns 3 and 4 of Table I. In the absence of grid Pulay and grid weight derivative terms, accurate Hessian calculations require the use of very fine integration grids (6–7) to even produce qualitatively reasonable results. Especially coarser grids yield extremely large errors for method **A′** with RMSD values of, e.g., 188 cm^{-1} for grid 4 and 847 cm^{-1} for grid 3; see Table I. However, inclusion of the two terms allows for similarly accurate results with significantly coarser grids (2–3). Consequently, the inclusion of the grid derivative terms becomes essential for reliable Hessian calculations when employing computationally reasonable grid sizes. Moreover, since the seminumerical approach only leads to a substantial speed-up in the evaluation of exchange integrals if coarser grids are used, the incorporation of grid derivative terms is indispensable in calculations of exact second derivatives of the seminumerical exchange energy, cf. Eq. (28).

The third method, denoted **B**, employs the approximation in Eq. (43) to obtain the second derivative exchange contributions to the Hessian. The results are presented in columns 5 and 6 of Table I for different grids. Qualitative agreement of the frequencies with the reference is only given for the finest grid 7. Even mid-sized grids (4–5) fail to predict the frequencies with large RMSD values of 335 and 46.4 cm^{-1}, respectively. These results are in agreement with the literature, stating that coarser grids are well-suited to approximate the gradient of seminumerical exchange integrals, while their second derivative can lead to pronounced errors.[32] However, since the applied approximation reduces the computational cost of the second derivative significantly, shown in Sec. II B 3, we decided to use a separate, very fine grid 8 for only the approximate second derivative seminumerical exchange term in Eq. (43). This scheme will be denoted method **C**. Grid 8 employs the same spherical integration grid as grid 7, but the radial grid is chosen to be finer. The resulting RMSD and MAD values in cm^{-1} are depicted in the last two columns of Table I for a variety of different grid sizes. Again, it should be stressed that for method **C**, the respective grid in Table I is only used for seminumerical exchange integrals and their first derivative, while the approximate second derivative term is calculated with the dedicated grid 8. The RMSD and MAD values are below 1 cm^{-1} for all grids under consideration, even for the very coarse grid 0. Therefore, a moderate scaling of the radial integration grid for the evaluation of second derivative exchange contributions seems sufficient to reproduce force constants for elements up to Ar.

1. Grid convergence for method C

The grid convergence of method **C** was further assessed for heavier elements. Ge_2H_6 was selected as a test system, as it is known to exhibit pronounced sensitivity to the choice of integration grid.[10,61] Table II summarizes the lowest three vibrational wavenumbers and the zero-point vibrational energy (ZPVE) obtained from

TABLE II. Three lowest wave numbers in cm^{-1} and ZPVE in E_h of Ge_2H_6 at the HF/def2-SVP level. Second derivative exchange contributions to the Hessian were evaluated using method **C** with the very fine grid 8, independent of the grid used elsewhere (grid 7). The radial grid size n_r of grid 8 was systematically increased.

n_r	n_{tot}[a]	$\tilde{\nu}_1(A_{1u})$	$\tilde{\nu}_1(A_{1g})$	$\tilde{\nu}_1(E_u)$	ZPVE
RF[b]	2 612 456	110.17	271.42	387.92	$48.748 \cdot 10^{-3}$
110	335 196	110.14	271.42	387.96	$48.748 \cdot 10^{-3}$
105	330 004	110.14	271.48	388.07	$48.751 \cdot 10^{-3}$
100	322 638	110.14	270.90	386.65	$48.723 \cdot 10^{-3}$
95	317 506	110.14	272.18	389.86	$48.785 \cdot 10^{-3}$
90	310 082	110.14	274.32	395.01	$48.885 \cdot 10^{-3}$
85	304 948	110.14	251.09	331.52	$47.764 \cdot 10^{-3}$
80	297 588	110.14	314.12	473.18	$50.702 \cdot 10^{-3}$

[a] Total number of grid points for the evaluation of second derivative exchange contributions.

[b] Reference values generated using exact derivatives, i.e., method **A**, in combination with reference grid RF.

force constant calculations for Ge_2H_6 at the HF/def2-SVP level of theory. Exchange integrals and their first derivatives were calculated using grid 7, while the second derivative seminumerical exchange contributions were calculated using method **C**, i.e., employing the accurate grid 8. The radial grid size n_r of grid 8 was systematically increased from 80 to 110. For comparison, reference data were generated using method **A**, i.e., using exact second derivatives of seminumerical exchange contributions, including grid Pulay and grid weight derivative terms, in combination with reference grid RF. Table II shows that quantitative agreement with the reference requires a larger radial grid for heavier elements. For the three vibrational modes considered, a radial grid size of $n_r = 105$ is necessary to achieve agreement within 1 cm^{-1}. With this grid, the ZPVE is accurate up to six digits. Smaller grids, e.g., $n_r = 80$, give large errors of up to 100 cm^{-1}. The best agreement with the reference is achieved with $n_r = 110$, which is, therefore, set as default for grid 8 for elements K–Kr.

TABLE III. Relative ZPVE errors in % and relative wall times for Ge_2H_6 at the HF/def2-SVP level. Second derivative exchange contributions to the Hessian were evaluated using both methods, **A** and **C**, across a range of grids.

Grid n	Method **A** $\Delta_{rel}(\text{ZPVE})$[a]	Method **C** $\Delta_{rel}(\text{ZPVE})$[a]	$t_{rel} = \frac{t_A(\text{grid } n)}{t_C}$[b]
7	$1.4 \cdot 10^{-3}$	$1.3 \cdot 10^{-3}$	17.28
6	$1.7 \cdot 10^{-3}$	$1.3 \cdot 10^{-3}$	9.79
5	$0.6 \cdot 10^{-3}$	$1.4 \cdot 10^{-3}$	6.89
4	$37.7 \cdot 10^{-3}$	$1.0 \cdot 10^{-3}$	4.01
3	$39.3 \cdot 10^{-3}$	$2.4 \cdot 10^{-3}$	2.41
2	$227.0 \cdot 10^{-3}$	$4.2 \cdot 10^{-3}$	1.40
1	$417.7 \cdot 10^{-3}$	$6.7 \cdot 10^{-3}$	1.04
0	$806.2 \cdot 10^{-3}$	$22.5 \cdot 10^{-3}$	0.79

[a] Relative ZPVE errors are defined with respect to the reference calculation (method **A**, grid RF).

[b] Relative wall times for the evaluation of second derivative exchange contributions obtained with method **A** with the corresponding integration grid, referenced to calculations using method **C**, which exhibits an almost constant timing t_C due to the fixed grid 8.

Table III reports the relative timings and relative errors of the ZPVE for Ge_2H_6 calculations at the same level of theory using different grid sizes. The second derivative seminumerical exchange contributions were evaluated with both, method **A** and **C**, where the latter uses grid 8 with $n_r = 110$. The relative ZPVE error in % is defined with respect to the reference calculation using method **A** in combination with reference grid RF. Relative wall times for the evaluation of second derivative exchange contributions, obtained using the exact expressions with the corresponding integration grid, i.e. method **A**, reference to calculations using method **C**. Note that the wall time t_C remains nearly constant because method **C** always uses grid 8 for the evaluation of the relevant terms. In all cases, except for the coarsest grid 0, the approximate scheme of method **C** requires shorter evaluation times than the exact scheme of method **A**. Remarkably, even for the coarsest grids, where both methods require a comparable computational effort, method **C** produces ZPVEs with errors of up to two orders of magnitude smaller than those obtained with method **A**. These results demonstrate that an accurate description of the second derivative exchange term is essential for reliable frequency calculations and requires rather large integration grids. Moreover, the proposed approximation offers a favorable balance of computational efficiency and accuracy when combined with the sufficiently large grid 8. In contrast, the use of coarser grids (0–1) for the evaluation of seminumerical exchange integrals and their first derivatives results in comparatively small errors, in agreement with previous reports.[32]

2. Benchmark of methods A and C for vibrational frequencies

Vibrational frequencies were further computed for a test set of 41 molecules at the B3LYP/def2-TZVP level of theory and employing both method **A** and method **C**. The RMSD and MAD of the vibrational frequencies are reported in Table IV for both methods and for a range of integration grids. Calculations using method **A** in combination with the large integration grid 7 serve as reference for the RMSD and MAD evaluation. The molecular orbitals for each molecule were obtained using grid 7 for seminumerical exchange and were kept fixed throughout all calculations in Table IV.

The present results are consistent with previous findings, showing that the RMSD of the vibrational frequencies obtained

TABLE IV. Root mean square deviations (RMSD) and mean absolute deviations (MAD) in cm^{-1} of vibrational frequencies for a test set of 41 molecules at the B3-LYP/def2-TZVP level, obtained using method **A** and method **C** to evaluate second derivative seminumerical exchange contributions to the Hessian across various integration grids. Vibrational frequencies generated using method **A** with grid 7 are used as reference for the RMSD and MAD values.

Grid	Method **A**		Method **C**	
	$\lvert\Delta\tilde{\nu}\rvert_{RMSD}$	$\lvert\Delta\tilde{\nu}\rvert_{MAD}$	$\lvert\Delta\tilde{\nu}\rvert_{RMSD}$	$\lvert\Delta\tilde{\nu}\rvert_{MAD}$
7	0	0	0.03	0.01
2	2.76	1.66	0.11	0.06
1	3.19	1.84	0.14	0.08
0	9.35	6.12	0.20	0.13

with method **C** remains below 1 cm^{-1} for all integration grids considered, with a maximum value of 0.20 cm^{-1} for grid 0. In contrast, method **A** exhibits significantly larger RMSD values, amounting, for example, to 2.76 cm^{-1} for grid 2. This demonstrates that an accurate evaluation of second derivative exchange contributions using method **A** requires larger integration grids, even with the grid weight derivatives being included.

To conclude, the approximation for the second derivative seminumerical exchange terms in Eq. (43) yields quantitatively reliable force constants. Achieving this accuracy requires the use of finer integration grids with increased radial grid sizes (method **C**), particularly for heavier elements. Nonetheless, the approximation still reduces computational cost, especially when the fine grid is applied only to the terms under consideration, in comparison with the exact evaluation of second derivative seminumerical exchange terms, including grid weight derivatives and grid Pulay terms (method **A**). Method **C** is used for the remainder of this work.

B. FDEu Hessian

The FDEu Hessian, introduced in Sec. II A 2, has been implemented in KOALA employing the DF-*J* and seminumerical exchange approximations discussed in the preceding sections for both HF and DFT. In the following, illustrative calculations of the FDEu Hessian are presented to demonstrate both the advantages and limitations of the method. We begin with a weakly coupled system to assess the performance of the FDEu approach in cases with small shifts of the vibrational frequencies due to the presence of environmental molecules. This is followed by calculations on strongly coupled systems, for which larger shifts are obtained.

1. Weakly coupled subsystems

As an initial test case for the new method, force constant calculations on formaldehyde in a tetrahedral sphere of four ethene molecules were performed at the B3LYP[62–64]/def2-TZVP[60] level of theory; see Fig. 2. This system was selected to illustrate weakly interacting subsystems, characterized by minor geometric coupling between the active system and the environment. Both a supermolecule and a FDEu calculation were performed, with formaldehyde as the active subsystem and ethene molecules as the frozen environment.

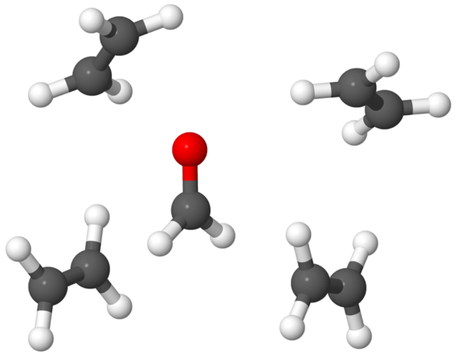

FIG. 2. Optimized geometry of the CH_2O $(C_2H_4)_4$ complex as obtained with TURBOMOLE using B3LYP/def2-TZVP/grid 4. Oxygen atoms are depicted in red, carbon atoms in gray, and hydrogen atoms in white.

TABLE V. Vibrational frequencies in cm^{-1} of CH_2O embedded in $(C_2H_4)_4$, at B3LYP/def2-TZVP level of theory, calculated for isolated CH_2O, the supermolecule, and using the FDEu approach.

Vibration	$\tilde{\nu}_{\text{isolated}}$	$\Delta\tilde{\nu}_{\text{supermol}}$[a]	$\Delta\tilde{\nu}_{\text{FDE}}$[b]	δ[c]
1	1203.52	−15.22	−1.89	13.33
2	1270.59	−8.94	+0.64	9.58
3	1530.81	−0.45	−0.56	0.11
4	1802.40	+2.79	+5.62	2.83
5	2902.46	+2.61	+3.71	1.10
6	2959.24	+10.36	+9.81	0.55

[a] $\Delta\tilde{\nu}_{\text{supermol}} = \tilde{\nu}_{\text{supermol}} - \tilde{\nu}_{\text{isolated}}$.

[b] $\Delta\tilde{\nu}_{\text{FDE}} = \tilde{\nu}_{\text{FDE}} - \tilde{\nu}_{\text{isolated}}$.

[c] Absolute FDEu error: $\delta = |\tilde{\nu}_{\text{FDE}} - \tilde{\nu}_{\text{supermol}}|$.

The resulting vibrational frequencies of formaldehyde are presented in Table V, including the isolated molecule as well as the frequency shifts for the supermolecule and the FDEu approach. Frequency shifts are defined relative to the vibrational frequencies of the isolated formaldehyde. The FDEu results are in good qualitative agreement with the supermolecule calculations for the higher-energy modes (3–6). For instance, FDEu captures 98% of the +10.36 cm^{-1} shift for the asymmetric stretching vibration at 2959.24 cm^{-1}.

By contrast, the low-lying bending vibrations (1–2) exhibit large shifts in the supermolecule calculation of −15.22 and −8.94 cm^{-1}, respectively, which are not accurately described by the FDEu approach. This discrepancy can be rationalized by the relatively flat potential energy surfaces associated with these modes, and it appears that these modes are particularly lacking the density response of the environment. However, the rather large deviations in the frequencies in cm^{-1} are caused by small changes in the Hessian. A vibrational shift of 1 cm^{-1} corresponds to a change of about $5 \cdot 10^{-6} E_\text{h}$ of Hessian matrix elements, which could be caused by lacking environment density response. Consequently, the deviations, which seem to be pronounced in case of the frequencies, lead only to an error of about 0.06 mE_h in the ZPVE, being as large as 26.6 mE_h in this case.

In the following, we turn to systems with stronger couplings between subsystems, where the ability of the FDEu method to describe, e.g., hydrogen bonds between different fragments is assessed.

2. Strongly coupled subsystems

To assess systems with strong inter-subsystem interactions, the water dimer was selected as a test system, as it incorporates hydrogen bonding. The first water molecule (D) acts as a hydrogen donor and the second one as a hydrogen acceptor (A). The vibrational frequencies of a water monomer, a supermolecule dimer, and a FDEu dimer calculation at the CAM-B3LYP[65]/def2-TZVPPD[66] level are presented in Table VI. Applying the FDEu approach, two different FDEu calculations need to be performed, with each of the water molecules acting as the active subsystem once. The corresponding vibrational spectrum is presented in Fig. 3. In comparison with the isolated water molecule, the presence of the hydrogen bridge in the dimer leads to a shift of the symmetric and asymmetric stretching modes of the hydrogen donor (D) to lower wave numbers,

TABLE VI. Vibrational frequencies in cm^{-1} of $(H_2O)_2$, at the CAM-B3LYP/def2-TZVPPD level of theory, calculated for an isolated water monomer, the supermolecule, and using the FDEu approach. The results for the latter two are given as vibrational shifts with respect to the vibrational frequencies of the isolated water monomer.

Vibration	$\tilde{\nu}_{\text{isolated}}$	$\Delta\tilde{\nu}_{\text{supermol}}$[a]	$\Delta\tilde{\nu}_{\text{FDE}}$[b]	δ[c]
$\tilde{\nu}_{\text{bend}}$ (D)[d]	1622.20	+0.77	+3.35	2.58
$\tilde{\nu}_{\text{bend}}$ (A)[e]		+20.98	+3.57	17.41
$\tilde{\nu}_{\text{sym}}$ (D)[d]	3849.53	−126.77	−78.64	48.13
$\tilde{\nu}_{\text{sym}}$ (A)[e]		−8.07	−9.25	1.18
$\tilde{\nu}_{\text{asym}}$ (D)[d]	3950.71	−27.51	−20.00	7.51
$\tilde{\nu}_{\text{asym}}$ (A)[e]		−11.90	−6.92	4.98

[a] $\Delta\tilde{\nu}_{\text{supermol}} = \tilde{\nu}_{\text{supermol}} - \tilde{\nu}_{\text{isolated}}$.

[b] $\Delta\tilde{\nu}_{\text{FDE}} = \tilde{\nu}_{\text{FDE}} - \tilde{\nu}_{\text{isolated}}$.

[c] Absolute FDEu error: $\delta = |\tilde{\nu}_{\text{FDE}} - \tilde{\nu}_{\text{supermol}}|$.

[d] Hydrogen donor (D).

[e] Hydrogen acceptor (A).

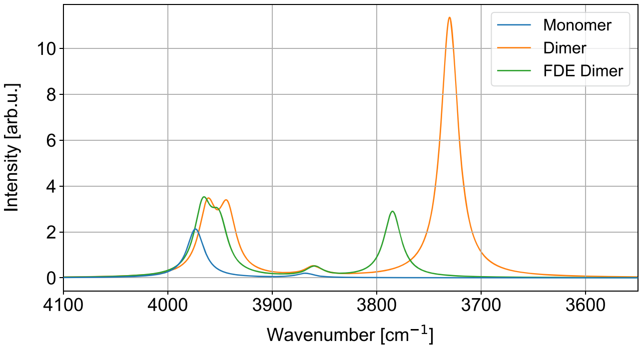

FIG. 3. Vibrational spectra in cm^{-1} of $(H_2O)_2$ at the CAM-B3LYP/def2-TZVPPD level of theory, calculated for the supermolecule and using the FDEu approach. The vibrational spectrum of a water monomer at the same level is also depicted.

cf. Table VI. On the one hand, the FDEu approach captures 62% of the shift of the symmetric stretching vibration of the hydrogen donor, while still exhibiting an absolute deviation of 48.13 cm^{-1}. On the other hand, it overestimates the shift of the symmetric stretching mode of the hydrogen acceptor, reproducing 115% of the −8.07 cm^{-1} shift. For the asymmetric stretching vibrations, the FDEu approach yields absolute errors of 7.51 and 4.98 cm^{-1} and recovers 73% and 58%, respectively, of the corresponding shifts obtained from the supermolecule calculation. In contrast, the bending vibrations associated with the hydrogen donor and hydrogen acceptor are shifted by +0.77 and +20.98 cm^{-1}, respectively, in the supermolecule calculation and exhibit a mode splitting that is not reproduced by the FDEu approach. Instead, both bending modes are shifted by nearly the same amount in the FDEu calculation, namely, +3.35 and +3.57 cm^{-1}. However, the deviations in the shifts lead only to an error of 0.1 mE_h in the ZPVE of 42.7 mE_h of the total system.

Consistent with findings for weakly coupled subsystems, cf. Sec. IV B 1, the FDEu approach does not properly describe the vibrational shifts of certain low-frequency bending modes. This deficiency is most likely due to the neglect of the environmental density response in the present FDEu treatment. Overall, the examples so far highlight the limitations of the FDEu approach: the electronic coupling between the two water molecules is not fully captured, which leads to pronounced absolute errors for specific vibrational modes, most notably the symmetric stretching vibration of the hydrogen donor. Nevertheless, the method correctly reproduces the qualitative environmental shifts for most vibrations, with the notable exception of the bending vibration of the hydrogen acceptor.

To evaluate the transferability of the observations made for the simple dimer to a larger system, a 4-aminophthalimide–water complex was investigated, cf. Fig. 4. This system incorporates multiple interfragment hydrogen bonds: the NH_2 fragment acts as hydrogen donor to the adjacent water molecule and one of the oxygen atoms acts as hydrogen acceptor for the other water molecule. Furthermore, the vibrations of the ring hydrogen atom adjacent to the water molecules are coupled to their movement. For this system, only vibrations of the active subsystem 4-aminophthalimide (4-AP) are discussed in the following. Vibrational spectra of the 4-AP molecule obtained from the supermolecule and the FDEu approach at the B3LYP/def2-TZVPPD level are presented in Fig. 5, while the respective frequency data are provided in the supplementary material. In the embedding calculations, 4-AP is treated as an active subsystem and the two water molecules constitute the environment. Frequencies of the isolated 4-AP molecule are given in the supplementary material for better comparability.

Overall, the vibrational frequencies of the supermolecule and the FDEu calculations show good agreement, yielding an RMSD of 10.04 cm^{-1}. Especially, the fingerprint region of the carbon ring structure is well-captured. Most frequencies deviate by less than 5 cm^{-1}, and only four of the 54 modes exhibit errors larger than 10 cm^{-1}. The largest deviations occur for the NH_2 group: the symmetric stretching vibration is off by 27.91 cm^{-1}, while the out-of-plane mode shows an error of 45.97 cm^{-1}. This

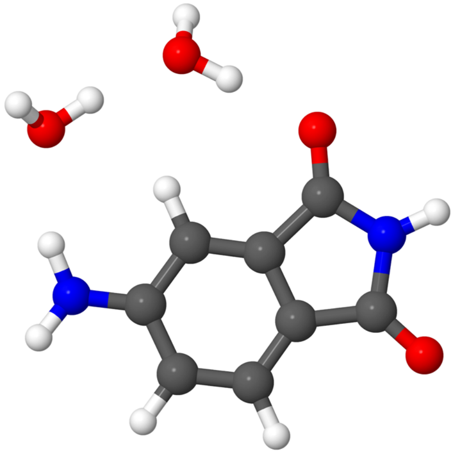

FIG. 4. Optimized ground-state geometry of the 4-aminophthalimide–water complex as obtained with TURBOMOLE using B3LYP/def2-TZVPPD/grid 4. Oxygen atoms are depicted in red, carbon atoms in gray, and hydrogen atoms in white.

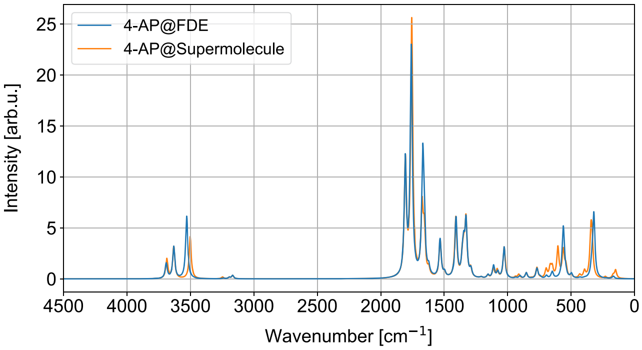

FIG. 5. Vibrational spectra in cm^{-1} of the 4-aminophthalimide molecule in the complex with two water molecules at the B3LYP/def2-TZVPPD level of theory, calculated employing the supermolecule and the FDEu approach.

fragment acts as a hydrogen donor toward the oxygen in the adjacent water molecule, cf. Fig. 4. However, the out-of-plane mode has the greatest shift of +118.94 cm^{-1} in the supermolecule for which the FDEu approach captures 61%, and the error in the total ZPVE of 132.8 mE_h is only 0.1 mE_h for the FDEu calculation. These results mirror the findings for the water dimer: geometric coupling across a hydrogen bond is not fully captured if the bond connects the active subsystem to the environment. Most vibrations of the system are well-described, but modes involving the hydrogen-bonded fragments exhibit pronounced absolute errors. As to be expected, the FDEu approach remains well-suited for describing local properties of a target subsystem, but stronger couplings are accounted for by incorporating the relevant molecules into the active region.

C. Embedded dimer

As a representative example for molecules in complex environments, a cutout of the molecular crystal structure of naphthalene was chosen, containing 44 naphthalene molecules with a total number of 792 atoms. The geometry is taken from crystallographic data,[67] and only the positions of the hydrogen atoms were reoptimized at the PBE/def2-SVP level; see Fig. 6. The naphthalene dimer at the center of the structure was chosen as the active system, with the environment depicted in light blue in Fig. 6. The active dimer was calculated at the PBE0[68]/def2-TZVP level, while the environment was treated at the PBE0/def2-SVP level. The vibrational spectrum in the range of 0–400 cm^{-1} of the naphthalene dimer embedded in the naphthalene crystal environment is presented in Fig. 7 and the data are given in the supplementary material. The dimer has three vibrations below 50 cm^{-1}. The lowest vibrational frequency is found to be 35.05 cm^{-1}, of which the normal mode is indicated by the arrows shown in Fig. 6. Furthermore, the normal modes at 43.46 and 197.75 cm^{-1} are illustrated in Fig. 8.

In order to apply our new method, we address the change of the frontier orbitals localized on the target subsystem upon vibrations of the respective subsystem. Both, local orbitals and local vibrations, are not straightforwardly accessible with supermolecular calculations, in particular as the cluster is no true minimum geometry as it is taken from the condensed phase.

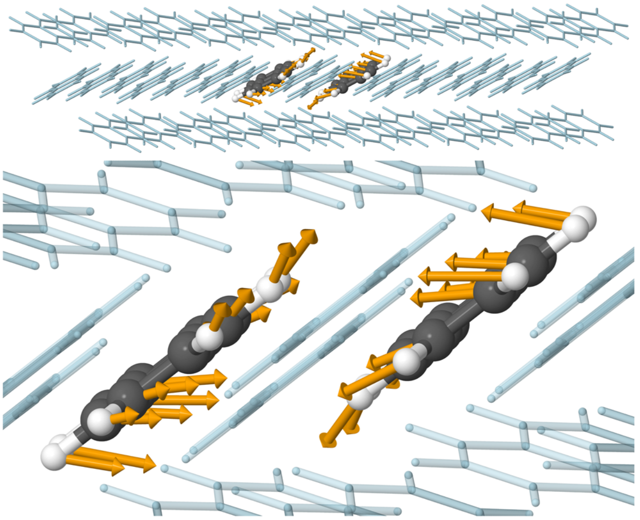

FIG. 6. Vibrational normal mode at 35.05 cm^{-1} inside a "6-stack" fragment of crystalline naphthalene. Carbon atoms of the active dimer are shown in gray, hydrogen atoms in white, and the surrounding environment in light blue.

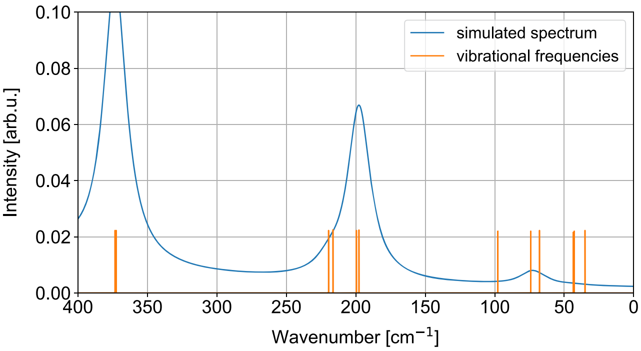

FIG. 7. Vibrational spectrum of a naphthalene dimer embedded in a cutout of crystalline naphthalene, zoomed to 0–400 cm^{-1}. The simulated spectrum is depicted in blue, generated with a FWHM of 1 cm^{-1}, and the computed eigenvalues of the molecular Hessian are shown in orange (neglecting intensity).

Displaced dimer geometries were generated following each normal mode with a certain amplitude, as given in Eq. (49). Table VII summarizes the nuclear repulsion energies, the highest occupied molecular orbital (HOMO) energies, and the energy gaps between the HOMO and the lowest unoccupied molecular orbital (LUMO) for the different displaced dimer geometries with FDE environment. An increase in the nuclear repulsion energy corresponds to a shorter intermolecular distance. Note that absolute values are given only for the reference geometry $\mathbf{R}_0$ in this table, while the values for the displaced geometries are given relative to those of $\mathbf{R}_0$.

For the lowest vibrational mode at 35.05 cm^{-1}, the vibrational temperature is 50 K and can thus be considered thermally active at room temperature. Its quantum mechanical amplitude x_quant is smaller than the thermal amplitude x_therm, so that the

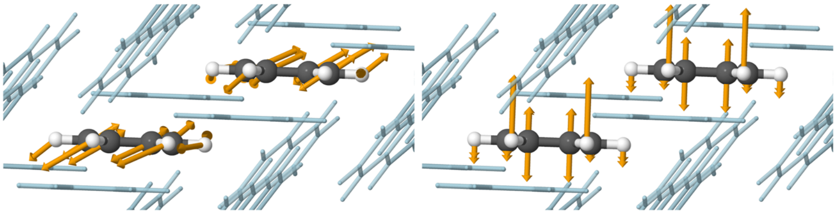

FIG. 8. Zoom onto selected vibration modes of a naphthalene dimer inside a "6-stack" fragment of crystalline naphthalene. The orange arrows indicate the normal mode at 43.46 cm^{-1} (left) and 197.75 cm^{-1} (right). Carbon atoms of the active dimer are shown in gray, hydrogen atoms in white, and the surrounding environment in light blue.

TABLE VII. Energies in eV for naphthalene dimer, 6 stack cf. Fig. 6, obtained at the PBE0/def2-TZVP level. Displaced geometries are generated following different normal modes, and the corresponding values are given relative to those of $\mathbf{R}_0$.

Mode[a]	Geometry	Nuc. rep.[b]	HOMO[c]	Gap[d]
	$\mathbf{R}_0$	1319.5	−6.264	5.083
35.05	$\mathbf{R}_0 - x_1^{\text{therm}}\,\mathbf{Q}_1$	+35.4	+0.090	−0.083
	$\mathbf{R}_0 + x_1^{\text{therm}}\,\mathbf{Q}_1$	−35.0	−0.047	+0.058
	Δ[e]	70.4	0.137	0.141
	$\mathbf{R}_0 - x_1^{\text{quant}}\,\mathbf{Q}_1$	+9.6	+0.019	−0.020
	$\mathbf{R}_0 + x_1^{\text{quant}}\,\mathbf{Q}_1$	−9.5	−0.016	+0.017
	Δ[e]	19.1	0.035	0.037
43.46	$\mathbf{R}_0 - x_3^{\text{therm}}\,\mathbf{Q}_3$	+7.4	−0.020	−0.058
	$\mathbf{R}_0 + x_3^{\text{therm}}\,\mathbf{Q}_3$	−13.1	+0.017	−0.084
	Δ[e]	20.5	0.037	0.026
	$\mathbf{R}_0 - x_3^{\text{quant}}\,\mathbf{Q}_3$	+3.0	−0.006	+0.017
	$\mathbf{R}_0 + x_3^{\text{quant}}\,\mathbf{Q}_3$	−3.6	+0.006	−0.026
	Δ[e]	6.6	0.012	0.043
197.75	$\mathbf{R}_0 - x_7^{\text{therm}}\,\mathbf{Q}_7$	−0.6	−0.015	−0.031
	$\mathbf{R}_0 + x_7^{\text{therm}}\,\mathbf{Q}_7$	−0.6	−0.015	−0.031
	Δ[e]	0.0	0.000	0.000
	$\mathbf{R}_0 - x_7^{\text{quant}}\,\mathbf{Q}_7$	−0.3	−0.007	−0.015
	$\mathbf{R}_0 + x_7^{\text{quant}}\,\mathbf{Q}_7$	−0.3	−0.007	−0.015
	Δ[e]	0.0	0.000	0.000

[a] Vibrational frequencies in cm^{-1}.

[b] Nuclear repulsion energy of the dimer without (w/o) environment, in Hartree.

[c] Energy of the highest occupied molecular orbital.

[d] Gap of HOMO and lowest unoccupied molecular orbital (LUMO).

[e] Absolute splitting of the respective electronic property around $\mathbf{R}_0$.

TABLE VIII. Selected modes of the naphthalene dimer, as embedded in the crystal environment.

Mode	Intensity[a]	T[b]	α_{HOMO}[c]	x_{therm}	x_{quant}
35.05	0.00	50	$-5.8 \cdot 10^{-4}$	3.525	1.022
43.46	0.00	62	$-2.9 \cdot 10^{-4}$	3.114	1.005
197.75	1.95	284	$+4.2 \cdot 10^{-7}$	0.750	0.516

[a] IR intensity in km/mol.

[b] Vibrational temperature in K.

[c] cf. Eq. (50).

resulting change in the frontier orbitals is also less pronounced, yielding a splitting of only 0.035 eV compared to the thermic splitting of 0.137 eV. The mode at 43.46 cm^{-1} exhibits analogous qualitative behavior. However, the corresponding thermal splitting of the HOMO energy is less pronounced and amounts to only 0.037 eV. Displacements along the mode at 197.75 cm^{-1} in both positive and negative directions do not induce a splitting of the HOMO energies around the equilibrium geometry $\mathbf{R}_0$ but rather lead to an overall constant shift. A similar behavior is found for the HOMO–LUMO gap, independent of whether thermal or quantum mechanical amplitudes are applied.

The directional derivatives α, cf. Eq. (50), are given in Table VIII, providing a first measure of the effect of vibrations on the thermal disorder. To obtain those, the orbital gradient of the HOMO[59] is multiplied by the respective dimensionless normalized normal mode $\mathbf{Q}_m$. The table reveals that the lowest vibrational mode exhibits the largest thermal and overall amplitude, and it also shows a significant change in the HOMO energy, cf. Table VII. This low-frequency mode is sometimes denoted "killer mode," as it induces large thermal fluctuations of the electronic coupling and thus dominates the dynamic disorder.[6] Interestingly, the mode at 43.46 cm^{-1} exhibits only slightly smaller values of both α_{HOMO} and x_{therm} compared to the mode at 35.05 cm^{-1}, while giving rise to a HOMO energy splitting that is smaller by approximately one order of magnitude.

To summarize, the new approach was used exemplarily to investigate the effect of local geometrical distortions upon orbitals, both localized on a target subsystems, achieved by the FDE approach. This approach, combining local orbitals and local vibrations, shows that, among the modes analyzed, the lowest vibration exhibits the largest modulation of the electronic properties under thermal displacement. Such a study is not straightforwardly possible with supermolecular methods.

V. CONCLUSIONS

In this work, we have reported the derivation of analytical nuclear second derivatives in the FDEu scheme for electronic ground states in the HF and DFT frameworks.

Exchange integrals and their derivatives are calculated using the COSX approximation. Different methods for the evaluation of second derivative exchange contributions to the Hessian were implemented and investigated. Only two methods, denoted **A** and **C** in the present work, produce accurate results compared with a reference calculation, where method **A** employs the exact second derivative of the seminumerical exchange energy, including grid weight derivatives and grid Pulay terms. Method **C** uses an approximation for the exact expression in method **A** in combination with a dedicated grid. This approximation requires finer integration grids with increased radial grid sizes, particularly for heavier elements, in order to yield quantitatively reliable force constants. Nonetheless, the approximation still reduces computational cost, especially when the fine grid is applied only to the terms under consideration, in comparison with method **A**. Future benchmarks comparing the efficiency of the approximation in method **C** with an exact treatment of second derivative exchange contributions are desirable.

Our implementation of the FDEu Hessian was used for a variety of different systems, which contain weakly and strongly coupled subsystems to show the limitations of the applied approach. As expected, the FDEu Hessian provides a reliable description of most vibrational frequencies for systems with only weak geometric coupling between different subsystems. However, certain environment-induced vibrational shifts are not fully captured by this approach, suggesting that the neglect of the density response of the environment can lead to noticeable errors for some specific vibrations. While most of the vibrations are quantitatively captured in systems containing hydrogen bonds in between different subsystems, pronounced errors occur for certain vibrations, typically the symmetric stretching vibration of the hydrogen donor. Such strong interactions should be explicitly accounted for in the FDEu approach by incorporating the relevant environment molecules into the active region.

Furthermore, we calculated the vibrational frequencies of a naphthalene dimer embedded in a cutout of the crystalline structure of naphthalene, containing 792 atoms. While such a dimer is not stable in vacuum without further constraints, the FDEu approach offers a suitable way to investigate local properties of dimers in molecular crystal environments. It also provides direct access to the vibrational frequencies of the subsystem of interest, enabling a conceptual-based localized interpretation of its (decoupled) modes. The new approach was applied to exemplarily investigate the influence of local vibrations on subsystem frontier orbitals and shall be used in future work to investigate charge-transport properties.

SUPPLEMENTARY MATERIAL

The supplementary material is provided in a separate file, containing details on the test set, integration grids, and vibrational frequencies of the calculations performed in Sec. IV.

ACKNOWLEDGMENTS

M.L.K. acknowledges financial support from the Deutsche Forschungsgemeinschaft (DFG) through the Research Training Group 2450 on "Tailored Scale-Bridging Approaches to Computational Nanoscience."

AUTHOR DECLARATIONS

Conflict of Interest

The authors have no conflicts to disclose.

Author Contributions

Maximilian L. Kronenberger: Conceptualization (equal); Data curation (equal); Formal analysis (equal); Investigation (equal); Methodology (equal); Software (equal); Validation (equal); Visualization (equal); Writing – original draft (equal); Writing – review & editing (equal). **Sebastian Höfener**: Conceptualization (equal); Data curation (equal); Formal analysis (equal); Funding acquisition (lead); Investigation (equal); Methodology (equal); Software (equal); Validation (equal); Visualization (equal); Writing – original draft (equal); Writing – review & editing (equal).

DATA AVAILABILITY

The data that support the findings of this study are available within the article and its supplementary material.

APPENDIX: DETAILS OF INTEGRAL EVALUATION

1. Coulomb density fitting DF-*J*

Starting from the two-electron integrals,

$$(\mu\nu|P) = \iint \mathrm{d}\mathbf{r}\mathrm{d}\mathbf{r}' \, \frac{\phi_\mu(\mathbf{r})\phi_\nu(\mathbf{r})\,\phi_P(\mathbf{r}')}{|\mathbf{r}-\mathbf{r}'|}, \tag{A1}$$

$$(Q|P) = \iint \mathrm{d}\mathbf{r}\mathrm{d}\mathbf{r}' \, \frac{\phi_Q(\mathbf{r})\phi_P(\mathbf{r}')}{|\mathbf{r}-\mathbf{r}'|}, \tag{A2}$$

and using the effective contraction,

$$\gamma_P = \sum_{\mu\nu} D_{\mu\nu}(\mu\nu|P), \tag{A3}$$

$$\Gamma_Q = \sum_P (Q|P)^{-1}\gamma_P, \tag{A4}$$

the second derivative of the DF-*J* energy without orbital rotation contributions is given as

$$\begin{aligned} E^{(\chi)(\xi)}_{\mathrm{DF}-J} &= \frac{1}{2}\sum_{\mu\nu}\sum_{\kappa\lambda} D_{\mu\nu}(\mu\nu|\kappa\lambda)^{(\chi)(\xi)}_{\mathrm{DF}} D_{\kappa\lambda}, &\text{(A5)}\\ &= \frac{1}{2}\sum_{PQ}\left[\gamma_P(P|Q)^{-1}\gamma_Q\right]^{(\chi)(\xi)}, &\text{(A6)}\\ &= \frac{1}{2}\sum_{PQ}\Bigg[2[\gamma_P]^{(\xi)}(P|Q)^{-1}\gamma_Q - \sum_{RS}\gamma_P(P|R)^{-1} \\ &\quad \times [(R|S)]^{(\xi)}(S|Q)^{-1}\gamma_Q\Bigg]^{(\chi)}, &\text{(A7)} \end{aligned}$$

where

$$\begin{aligned} &\frac{1}{2}\sum_{PQ}\left[2[\gamma_P]^{(\xi)}(P|Q)^{-1}\gamma_Q\right]^{(\chi)} \\ &\quad = \sum_P [\gamma_P]^{(\xi)(\chi)}\Gamma_P + \sum_{PQ}[\gamma_P]^{(\xi)}(P|Q)^{-1}[\gamma_Q]^{(\chi)} \\ &\qquad - \sum_{PQ}\sum_{RS}[\gamma_P]^{(\xi)}(P|R)^{-1}[(R|S)]^{(\chi)}\Gamma_S \end{aligned} \tag{A8}$$

and

$$\frac{1}{2}\sum_{PQ}\left[-\sum_{RS}\gamma_P(P|R)^{-1}[(R|S)]^{(\xi)}(S|Q)^{-1}\gamma_Q\right]^{(\chi)}$$
$$= -\sum_{PQR}[\gamma_P]^{(\chi)}(P|Q)^{-1}[(Q|R)]^{(\xi)}\Gamma_R$$
$$-\frac{1}{2}\sum_{PQ}\Gamma_P[(P|Q)]^{(\chi)(\xi)}\Gamma_Q$$
$$+\sum_{PQRS}\Gamma_P[(P|Q)]^{(\chi)}(Q|R)^{-1}[(R|S)]^{(\xi)}\Gamma_S. \tag{A9}$$

Here, we have used upper indices in parentheses for all terms to stress that no orbital coefficients need to be differentiated for these contributions. The full derivative contains orbital rotation contributions, which are contained in other terms in Eq. (20).

2. Range separation

In case of range separation, the exchange energy is computed from a screened Coulomb potential, and the integrals in Eq. (29) then become[69]

$$E_{rs-K,\,\mathrm{sem}} = -\frac{1}{4}c_{\mathrm{x}}\sum_{\mu\nu\kappa\lambda} D_{\mu\nu}D_{\kappa\lambda}(\mu\kappa|s|\nu\lambda)_{\mathrm{sem}}, \tag{A10}$$

where the two-electron integral is approximated as follows:

$$(\mu\kappa|s|\nu\lambda)_{\mathrm{sem}} = \sum_g w_g\,\phi_{\mu g}\,\phi_{\kappa g}(\nu|s|\lambda)_g, \tag{A11}$$

with the range-separated one-electron integral,

$$(\nu|s|\lambda)_g = \int \mathrm{d}\mathbf{r}\,\phi_\nu(\mathbf{r})\frac{\alpha + \beta\,\mathrm{erf}(\eta\,|\mathbf{r}-\mathbf{r}_g|)}{|\mathbf{r}-\mathbf{r}_g|}\phi_\lambda(\mathbf{r}), \tag{A12}$$

where α, β, and η are parameters that are defined in combination with the chosen functional.

REFERENCES

[1] H. Bronstein, C. B. Nielsen, B. C. Schroeder, and I. McCulloch, Nat. Rev. Chem. **4**, 66 (2020).

[2] V. Coropceanu, J. Cornil, D. A. da Silva Filho, Y. Olivier, R. Silbey, and J.-L. Brédas, Chem. Rev. **107**, 926 (2007).

[3] H. Sirringhaus, Adv. Mater. **26**, 1319 (2014).

[4] J. Panidi, A. F. Paterson, D. Khim, Z. Fei, Y. Han, L. Tsetseris, G. Vourlias, P. A. Patsalas, M. Heeney, and T. D. Anthopoulos, Adv. Sci. **5**, 1700290 (2018).

[5] A. W. Hains, Z. Liang, M. A. Woodhouse, and B. A. Gregg, Chem. Rev. **110**, 6689 (2010).

[6] G. Schweicher, G. D'Avino, M. T. Ruggiero, D. J. Harkin, K. Broch, D. Venkateshvaran, G. Liu, A. Richard, C. Ruzié, J. Armstrong, A. R. Kennedy, K. Shankland, K. Takimiya, Y. H. Geerts, J. A. Zeitler, S. Fratini, and H. Sirringhaus, Adv. Mater. **31**, 1902407 (2019).

[7] M. A. Dettmann, L. S. R. Cavalcante, C. A. Magdaleno, and A. J. Moulé, Adv. Funct. Mater. **33**, 2213370 (2023).

[8] J. A. Pople, R. Krishnan, H. B. Schlegel, and J. S. Binkley, Int. J. Quantum Chem. **16**, 225 (1979).

[9] Y. Osamura, Y. Yamaguchi, and H. F. Schaefer, Chem. Phys. **103**, 227 (1986).

[10] P. Deglmann, F. Furche, and R. Ahlrichs, Chem. Phys. Lett. **362**, 511 (2002).

[11] P. Jørgensen and T. Helgaker, J. Chem. Phys. **89**, 1560 (1988).

[12] T. Helgaker, P. Jørgensen, and N. C. Handy, Theor. Chim. Acta **76**, 227 (1989).

[13] H. Koch, H. J. A. Jensen, P. Jørgensen, T. Helgaker, G. E. Scuseria, I. Schaefer, and F. Henry, J. Chem. Phys. **92**, 4924 (1990).

[14] D. H. Friese, C. Hättig, and J. Komann, J. Chem. Theory Comput. **9**, 1469–1480 (2013).

[15] A. Ghysels, H. L. Woodcock III, J. D. Larkin, B. T. Miller, Y. Shao, J. Kong, D. V. Neck, V. V. Speybroeck, M. Waroquier, and B. R. Brooks, J. Chem. Theory Comput. **7**, 496–514 (2011).

[16] F. Lipparini, C. Cappelli, G. Scalmani, N. De Mitri, and V. Barone, J. Chem. Theory Comput. **8**, 4270–4278 (2012).

[17] J. Vester and J. M. H. Olsen, J. Chem. Theory Comput. **20**, 9533–9546 (2024).

[18] P. T. Panek and C. R. Jacob, ChemPhysChem **15**, 3365 (2014).

[19] C. König, M. B. Hansen, I. H. Godtliebsen, and O. Christiansen, J. Chem. Phys. **144**, 074108 (2016).

[20] J. Hellmers and C. König, J. Chem. Phys. **159**, 104108 (2023).

[21] T. A. Wesolowski and A. Warshel, J. Phys. Chem. **97**, 8050 (1993).

[22] A. S. P. Gomes and C. R. Jacob, Annu. Rep. Prog. Chem., Sect. C: Phys. Chem. **108**, 222 (2012).

[23] T. A. Wesolowski, S. Shedge, and X. Zhou, Chem. Rev. **115**, 5891 (2015).

[24] C. R. Jacob and J. Neugebauer, Wiley Interdiscip. Rev.: Comput. Mol. Sci. **4**, 325 (2014).

[25] C. R. Jacob and J. Neugebauer, Wiley Interdiscip. Rev.: Comput. Mol. Sci. **14**, e1700 (2024).

[26] J. Heuser and S. Höfener, J. Comput. Chem. **37**, 1092 (2016).

[27] T. A. Wesołowski, A. Goursot, and J. Weber, J. Chem. Phys. **115**, 4791 (2001).

[28] M. Iannuzzi, B. Kirchner, and J. Hutter, Chem. Phys. Lett. **421**, 16–20 (2006).

[29] M. Dułak, J. W. Kamiński, and T. A. Wesołowski, J. Chem. Theory Comput. **3**, 735–745 (2007).

[30] F. Neese, F. Wennmohs, A. Hansen, and U. Becker, Chem. Phys. **356**, 98 (2009).

[31] R. Izsák and F. Neese, J. Chem. Phys. **135**, 144105 (2011).

[32] D. Bykov, T. Petrenko, R. Izsák, S. Kossmann, U. Becker, E. Valeev, and F. Neese, Mol. Phys. **113**, 1961 (2015).

[33] C. Holzer, J. Chem. Phys. **153**, 184115 (2020).

[34] B. Helmich-Paris, B. de Souza, F. Neese, and R. Izsák, J. Chem. Phys. **155**, 104109 (2021).

[35] P. Plessow and F. Weigend, J. Comput. Chem. **33**, 810–816 (2012).

[36] Y. Won, J.-G. Lee, M. N. Ringnalda, and R. A. Friesner, J. Chem. Phys. **94**, 8152 (1991).

[37] T. Petrenko, S. Kossmann, and F. Neese, J. Chem. Phys. **134**, 054116 (2011).

[38] H. Laqua, J. C. B. Dietschreit, J. Kussmann, and C. Ochsenfeld, J. Chem. Theory Comput. **18**, 6010 (2022).

[39] A. S. P. Gomes, C. R. Jacob, and L. Visscher, Phys. Chem. Chem. Phys. **10**, 5353 (2008).

[40] S. Höfener, A. Severo Pereira Gomes, and L. Visscher, J. Chem. Phys. **136**, 044104 (2012).

[41] J. Heuser and S. Höfener, J. Comput. Chem. **38**, 2316 (2017).

[42] N. C. Handy, D. J. Tozer, G. J. Laming, C. W. Murray, and R. D. Amos, Isr. J. Chem. **33**, 331 (1993).

[43] B. G. Johnson and M. J. Fisch, J. Chem. Phys. **100**, 7429 (1994).

[44] E. R. Davidson, J. Chem. Phys. **17**, 87 (1975).

[45] B. G. Johnson, P. M. W. Gill, and J. A. Pople, J. Chem. Phys. **98**, 5612 (1993).

[46] O. Treutler and R. Ahlrichs, J. Chem. Phys. **102**, 346 (1995).

[47] A. D. Becke, J. Chem. Phys. **88**, 2547 (1988).

[48] V. I. Lebedev, USSR Comput. Math. Math. Phys. **15**, 44 (1975).

[49] V. I. Lebedev, USSR Comput. Math. Math. Phys. **16**, 10 (1976).

[50] V. I. Lebedev, Sib. Math. J. **18**, 99–107 (1977).

[51] S. Grimme, M. Steinmetz, and M. Korth, J. Org. Chem. **72**, 2118–2126 (2007).

[52] F. Neese, A. Hansen, F. Wennmohs, and S. Grimme, Acc. Chem. Res. **42**, 641–648 (2009).

[53] S. Höfener, Int. J. Quantum Chem. **121**, e26351 (2021).

[54] J. P. Perdew, K. Burke, and M. Ernzerhof, Phys. Rev. Lett. **77**, 3865 (1996).

[55] A. Lembarki and H. Chermette, Phys. Rev. A **50**, 5328 (1994).

[56] O. Vahtras, J. Almlöf, and M. Feyereisen, Chem. Phys. Lett. **213**, 514 (1993).

[57] F. Weigend, Phys. Chem. Chem. Phys. **8**, 1057 (2006).

[58] Y. J. Franzke, C. Holzer, J. H. Andersen, T. Begušić, F. Bruder, S. Coriani, F. Della Sala, E. Fabiano, D. A. Fedotov, S. Fürst, S. Gillhuber, R. Grotjahn,

M. Kaupp, M. Kehry, M. Krstić, F. Mack, S. Majumdar, B. D. Nguyen, S. M. Parker, F. Pauly, A. Pausch, E. Perlt, G. S. Phun, A. Rajabi, D. Rappoport, B. Samal, T. Schrader, M. Sharma, E. Tapavicza, R. S. Treß, V. Voora, A. Wodyński, J. M. Yu, B. Zerulla, F. Furche, C. Hättig, M. Sierka, D. P. Tew, and F. Weigend, J. Chem. Theory Comput. **19**, 6859 (2023).

[59] J. Weissert, A. C. Ellinger, and S. Höfener, J. Phys. Chem. A **129**, 7715–7728 (2025).

[60] F. Weigend and R. Ahlrichs, Phys. Chem. Chem. Phys. **7**, 3297 (2005).

[61] J. M. L. Martin, C. W. Bauschlicher, and A. Ricca, Comput. Phys. Commun. **133**, 189 (2001).

[62] A. D. Becke, J. Chem. Phys. **98**, 5648 (1993).

[63] C. Lee, W. Yang, and R. G. Parr, Phys. Rev. B **37**, 785 (1988).

[64] P. J. Stephens, F. J. Devlin, C. F. Chabalowski, and M. J. Frisch, J. Phys. Chem. **98**, 11623 (1994).

[65] T. Yanai, D. P. Tew, and N. C. Handy, Chem. Phys. Lett. **393**, 51–57 (2004).

[66] D. Rappoport and F. Furche, J. Chem. Phys. **133**, 134105 (2010).

[67] F. P. A. Fabbiani, D. R. Allan, S. Parsons, and C. R. Pulham, Acta Crystallogr., Sect. B: Struct. Sci. **62**, 826–842 (2006).

[68] J. P. Perdew, M. Ernzerhof, and K. Burke, J. Chem. Phys. **105**, 9982 (1996).

[69] M. T. Wachter-Lehn, K. Fink, and S. Höfener, J. Chem. Phys. **157**, 134109 (2022).